

LCD-Note-2011-003

## Determination of Chargino and Neutralino Masses in high-mass SUSY scenarios at CLIC

N. Alster\* † and M. Battaglia\* †

\* *University of California at Santa Cruz, Santa Cruz, CA, USA* † *CERN, Geneva, Switzerland,*

March 11, 2011

### Abstract

This note reports the results of a study of the accuracy in the determination of chargino and neutralino masses in two high-mass supersymmetric scenarios through kinematic endpoints and threshold scans at a multi-TeV  $e^+e^-$  collider. The effects of initial state radiation, beamstrahlung and parton energy resolution are studied in fully hadronic final states of inclusive SUSY samples. Results obtained at generator level are compared to those from fully simulated and reconstructed events for selected channels.

# 1 Introduction

The study of the gaugino sector of Supersymmetry is a complex and important endeavour, which appears well suited to a linear collider of sufficient energy and luminosity. The main observables of interest are the masses of the  $\chi^0$  and  $\chi^\pm$  states and their production cross sections, including those with polarised beams.  $e^+e^-$  collisions offer two independent techniques for determining the mass of supersymmetric particles. These are the analysis of the energy spectrum of the SM particle produced in association with a lighter supersymmetric state in the two-body decays and the study of the pair production cross section near threshold. These techniques have already been extensively studied for lower centre-of-mass energies,  $\sqrt{s}$ , between 0.35 to 0.5 TeV [1–4]. In this note, we analyse the gaugino pair production and derive the statistical accuracy on their masses using both techniques and including the effects of initial state radiation (ISR), beamstrahlung (BS) and parton energy resolution for multi-TeV  $e^+e^-$  collisions. We follow the evolution of these accuracies for fully hadronic final states from pure signal samples to realistic inclusive SUSY samples and validate the results obtained at generator level with analyses performed on fully simulated and reconstructed events. The study provides us with requirements on parton energy resolution which are complementary to those obtained from other processes, such as heavy SUSY Higgs decays, since the kinematics of decays of gaugino pairs with large missing energy into pairs of escaping neutralinos does not benefit from the kinematic fits, which are instead applicable to processes where the full beam energy is deposited in the detector. The estimated mass accuracies can be compared in a next step to those required for the reconstruction of the GUT scale SUSY parameters [5] and the determination of the lightest neutralino contribution to the dark matter relic density in the universe [6]. This comparison will provide us with well-motivated quantitative requirements on parton energy resolution in SUSY events.

## 2 SUSY Models

This study considers two scenarios in the constrained MSSM (cMSSM) model, which offer different experimental challenges. Their parameters are given in Table 1. The first (model I), adopted as a benchmark point for the CLIC CDR studies [7], has the lightest neutralino at 340 GeV and the chargino and heavier neutralinos with masses in the range 640 to 917 GeV (see Table 2 and the left panel of Figure 1). At  $\sqrt{s} = 3$  TeV all the gauginos are observables. The relatively low masses and the 3 TeV centre-of-mass energy make cross sections sizable but the beamstrahlung effects more significant (see Table 1). In the second (model II<sup>1</sup>) the lightest neutralino has a mass of 554 GeV, while the other neutralinos and the charginos have masses in the range from 1064 to 1414 GeV (see Table 2 and the right panel of Figure 1) [8]. At 3 TeV, most gauginos are close to threshold for pair production and cross sections are small. This minimises the beamstrahlung effects, since the production cross section drops significantly when the beams lose energy due to radiation. The cross sections are given in Table 3 and Figure 2.

The main features of these two models of interest in this study are the large sparticle masses and the dominance of decays through  $W^\pm$ ,  $h^0$  and, to a lesser extent,  $Z^0$  bosons. These features are common to most of the large-tan  $\beta$  cMSSM models [9] with neutralino dark matter

---

<sup>1</sup>This is point K' of ref [8].

Table 1: Parameters of the two cMSSM models adopted in this study

Parameter	Model I	Model II
$m_0$ (GeV)	966	1001
$m_{1/2}$ (GeV)	800	1300
$\tan\beta$	51	46
$A_0$	0.	0.
$\text{sgn}(\mu)$	+	-
$m_{top}$ (GeV)	173.3	175

Table 2: Gaugino mass spectrum in the two cMSSM models adopted in this study

Particle	Mass (GeV)	Width (GeV)	Mass (GeV)	Width (GeV)
$\chi_1^0$	340.3	-	554.3	-
$\chi_2^0$	643.2	0.02	1064.2	0.04
$\chi_3^0$	905.5	4.55	1407.2	6.75
$\chi_4^0$	916.7	4.64	1413.8	6.85
$\chi_1^\pm$	643.2	0.02	1064.3	0.04
$\chi_2^\pm$	916.7	4.63	1413.7	8.08

compatible with the Cosmic Microwave Background (CMB) data. We verify this by performing scans of the cMSSM parameter space around both benchmark points to examine the mass spectrum and decay branching fractions of gauginos. In these scans we vary  $m_0$  and  $m_{1/2}$  within  $\pm 300$  GeV from the benchmark parameters,  $\tan\beta$  within  ${}_{-15}^{+5}$ ,  $A_0$  within  $\pm 250$  and  $\mu$  to have

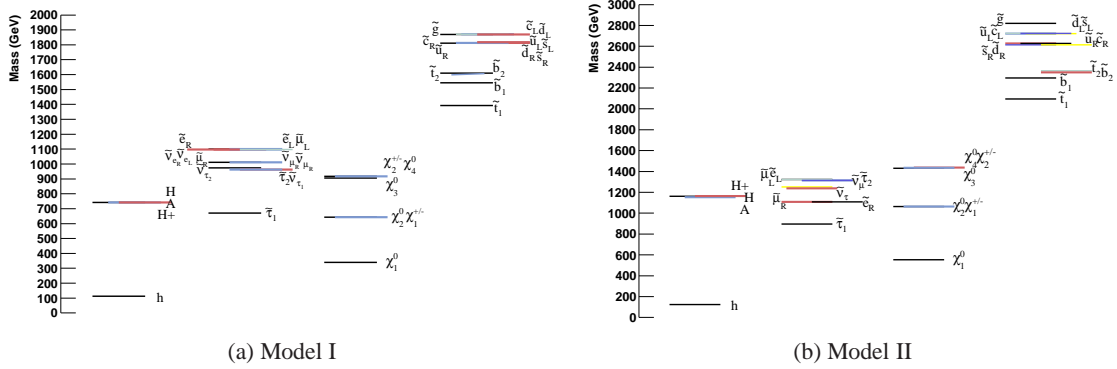
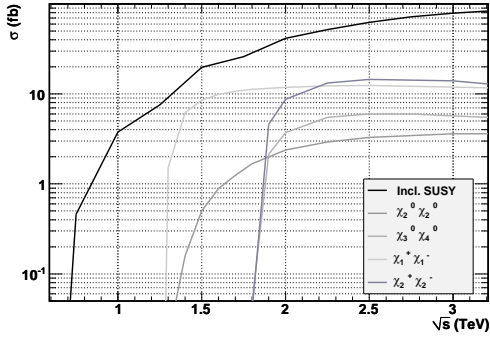


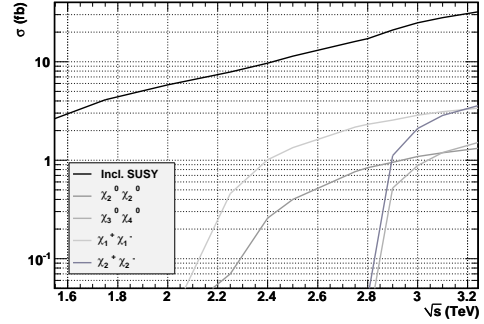
Figure 1: Supersymmetric particle spectra for Model I and II.

Table 3: Cross sections for gaugino pair production in the two cMSSM models adopted in this study

Process	no Rad (fb)	ISR (fb)	ISR+BS (fb)	Pol +0.8/0.0 (fb)	Pol +0.8/-0.6 (fb)
<b>Model I</b>					
Inclusive SUSY	103.3	97.4	79.3		
$e^+e^- \rightarrow \chi_1^+ \chi_1^-$	11.5	11.6	11.9	21.4	34.0
$e^+e^- \rightarrow \chi_2^0 \chi_2^0$	4.2	4.1	3.6	6.5	10.4
$e^+e^- \rightarrow \chi_2^+ \chi_2^-$	14.5	14.4	13.8	21.1	33.3
$e^+e^- \rightarrow \chi_3^0 \chi_4^0$	6.1	6.1	6.0	6.8	10.3
<b>Model II</b>					
Inclusive SUSY	45.4	39.0	25.2		
$e^+e^- \rightarrow \chi_1^+ \chi_1^-$	4.9	4.3	2.9	5.2	8.3
$e^+e^- \rightarrow \chi_2^0 \chi_2^0$	1.9	1.7	1.1	2.0	3.1
$e^+e^- \rightarrow \chi_2^+ \chi_2^-$	6.2	4.6	2.1	3.2	5.1
$e^+e^- \rightarrow \chi_3^0 \chi_4^0$	2.6	2.0	0.9	1.0	1.5



(a) Model I



(b) Model II

Figure 2: Cross sections for gaugino pair production vs.  $\sqrt{s}$  in (left) model I and (right) model II

either sign. The sparticle spectrum corresponding to each set of parameters is computed using SUSPECT 2.2 [10] and the decay branching ratios with SDECAY 1.3 [11]. We compute the neutralino relic density,  $\Omega_\chi$ , using Micromegas 2.2 [12]. In total, we generate over 150k cMSSM points using a flat sampling of the parameter phase space. Of these, we retain those points consistent with the current limits on the lightest Higgs bosons and sparticle masses and yielding  $0.093 < \Omega_\chi/h^2 < 0.129$ , in agreement with the WMAP seven-years data [13]. Figure 3 shows the  $\chi_1^\pm$  mass and Figure 4 the  $\chi_1^\pm \rightarrow W^\pm \chi_1^0$  branching fraction for the accepted points. These results show that decays into bosons are dominant in this region of the cMSSM parameter space. These results can be extended to the general MSSM where a significant fraction of

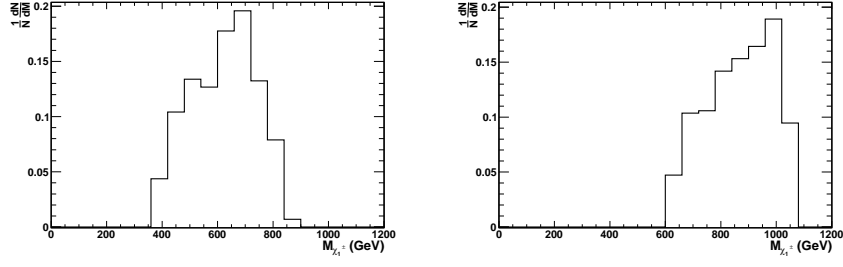


Figure 3: Distribution of  $\chi_1^\pm$  mass values for points compatible with WMAP data from the cMSSM scan around (left) model I and (right) model II.

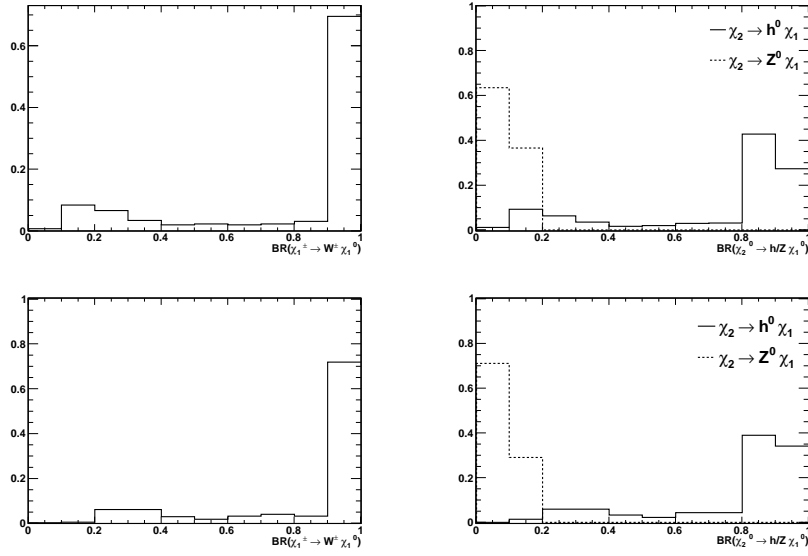


Figure 4: Distribution of branching fraction values for (left)  $\chi_1^\pm \rightarrow W^\pm \chi_1^0$  and (right)  $\chi_2^0 \rightarrow h^0 \chi_1^0$ ,  $Z^0 \chi_1^0$  for points compatible with WMAP data from the cMSSM scan around (upper row) model I and (lower row) model II, showing the predominance of decays into bosons.

the decays of  $\chi_1^\pm$  and  $\chi_2^0$  and the majority of those of the heavier chargino and neutralinos are two-body processes with emission of a boson. In these scenarios,  $W^\pm$ ,  $Z^0$  and  $h^0$  production is a distinctive signature of gaugino decays. Figure 5 shows the boson mass spectrum at generator level in inclusive SUSY events for the two models considered in this study, showing the  $W^\pm$ ,  $Z^0$  and  $h^0$  boson contribution. The  $W/Z/h$  discrimination is essential for identifying the decay processes, which sets constraints on parton energy resolution through the di-jet invariant mass resolution. Precise parton energy reconstruction is similarly required to preserve the accuracy in the gaugino mass measurements through the determination of the endpoints of the boson energy

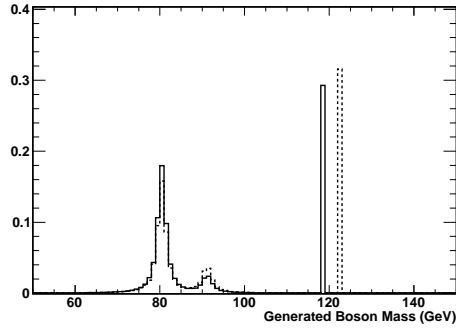


Figure 5: Boson spectrum in inclusive SUSY events with  $\geq 4$  jets + missing energy for model I (continuous line) and II (dashed line). The  $h^0$  mass is 118.5 and 122.9 GeV, respectively.

spectra.

## 2.1 Event Simulation

For this study, events are generated with PYTHIA 6.215 [14]. For model I the SUSY spectrum and the sparticle decay branching fractions are forced to those obtained with SUSPECT 2.2 and SDECAY 1.3, respectively. For model II the spectrum is generated with ISASUGRA 7.69 [15]. Polarised cross sections are obtained using SUSYGEN 3.0 [16]. The production cross sections for unpolarised and polarised beams are summarised in Table 3. Samples of inclusive SUSY events are processed through full detector simulation using the GEANT-4-based MOKKA [17] program and reconstructed with MARLIN-based [18] processors for a version of the ILD detector concept [2], modified for physics at CLIC [19]. These events are used for a validation of the results in the 4-jet,  $WW$  and  $hh$  final states, discussed in section 3.3.5.

## 3 Mass Determination by Fits to Boson Energy Spectra

In the two body decay process  $A \rightarrow BC$  into a boson  $B$  and a lighter gaugino,  $C$ , which are a signature of these high-mass benchmark points, the masses of the parent and daughter gauginos can be extracted from the position of the kinematic edges of the boson energy spectrum. The technique was first proposed for squarks [20] and later extended to other sparticles in two-body decays [21]. In the case of gaugino decays into bosons, their mass,  $m_B$ , cannot be neglected, as in the case of squark and slepton decays and the relation between the energy endpoint and the masses of the particle involved in the decay process are given by:

$$E_{\text{BH,BL}} = \gamma(E_B^* \pm \beta E_B^*) \quad (1)$$

where

$$E_B^* = \frac{m_A^2 + m_B^2 - m_C^2}{2m_A} \quad (2)$$

$$\gamma = \frac{\sqrt{s}}{2m_A} \quad (3)$$

$$\beta = \sqrt{\frac{1 - 4m_A^2}{s}} \quad (4)$$

These formulae can be extended in a straightforward way to the case in which the gaugino  $A$  is not directly produced in the  $e^+e^-$  collisions but originates from the decay of an heavier particle,  $A'$ , by replacing  $s$  with  $E_A^2$ , where  $E_A$  is its energy. In the case of cascading decays  $A' \rightarrow AB' \rightarrow BC$ ,  $E_A$  is obtained as  $\sqrt{s} - E_{B'H} < E_A < \sqrt{s} - E_{B'L}$ .

### 3.1 Channels

We study the following processes <sup>2)</sup> for model I:

- $e^+e^- \rightarrow \chi_1^+ \chi_1^- \rightarrow W^+ \chi_1^0 W^- \chi_1^0; W \rightarrow q\bar{q}'$ ,
- $e^+e^- \rightarrow \chi_2^0 \chi_2^0 \rightarrow h^0 \chi_1^0 h^0 \chi_1^0; h \rightarrow b\bar{b}$ ,
- $e^+e^- \rightarrow \chi_2^+ \chi_2^+ \rightarrow W^+ \chi_2^0 W^- \chi_1^0 \rightarrow W^+ h^0 \chi_1^0 W^- \chi_1^0; h \rightarrow b\bar{b}, W \rightarrow q\bar{q}'$ ,
- $e^+e^- \rightarrow \chi_2^+ \chi_2^+ \rightarrow h^0 \chi_1^+ W^- \chi_1^0 \rightarrow h^0 W^+ \chi_1^0 W^- \chi_1^0; h \rightarrow b\bar{b}, W \rightarrow q\bar{q}'$ ,
- $e^+e^- \rightarrow \chi_2^+ \chi_2^+ \rightarrow Z^0 \chi_1^+ W^- \chi_1^0 \rightarrow Z^0 W^+ \chi_1^0 W^- \chi_1^0; Z \rightarrow q\bar{q}, W \rightarrow q\bar{q}'$ ,
- $e^+e^- \rightarrow \chi_4^0 \chi_3^0 \rightarrow W^+ \chi_1^- W^- \chi_1^+ \rightarrow W^+ W^- \chi_1^0 W^- W^+ \chi_1^0; W \rightarrow q\bar{q}'$ .

For model II we study:

- $e^+e^- \rightarrow \chi_1^+ \chi_1^- \rightarrow W^+ \chi_1^0 W^- \chi_1^0; W \rightarrow q\bar{q}'$
- $e^+e^- \rightarrow \chi_2^0 \chi_2^0 \rightarrow h^0 \chi_1^0 h^0 \chi_1^0; h \rightarrow b\bar{b}$ .

They explore increasing event complexities from 4-jet with two bosons to eight jets with four bosons. Mass values and their statistical uncertainties are extracted by a binned  $\chi^2$  fit using the `Minuit` package [22]. The boson energy spectrum from simulation is compared to reference spectra generated according to Eq.(1) above, changing the sparticle masses. An integrated luminosity of  $2 \text{ ab}^{-1}$  is assumed. The  $\sqrt{s}$  value in Eq.(4) is either kept to the nominal value of 3 TeV or smeared to account for ISR and beamstrahlung effects, as discussed below. Since the fit procedures requires to generate a large number of reference spectra, which are statistically independent, in the fitter iterations, each of these is filled with  $2.5 \times 10^6$  random entries distributed according to Eq.(1), to minimise effects from their statistical fluctuations in the `Minuit` calculations, in particular in the determination of the derivatives.

---

<sup>2)</sup>Throughout the paper the charge conjugate of the given state is also implied

### 3.2 Effect of Beam Spectra and Energy Resolution

The effects of initial state radiation (ISR), beamstrahlung (BS) and finite resolution in parton energy reconstruction are taken into account. Beamstrahlung effects on the luminosity spectrum are included using results of the CLIC beam simulation for the 2008 accelerator parameters [23]. Initial state radiation is included in the event generation in PYTHIA. The beamstrahlung spectrum obtained is then used for smearing the  $\sqrt{s}$  value in Eq. 4. We model the ISR spectrum

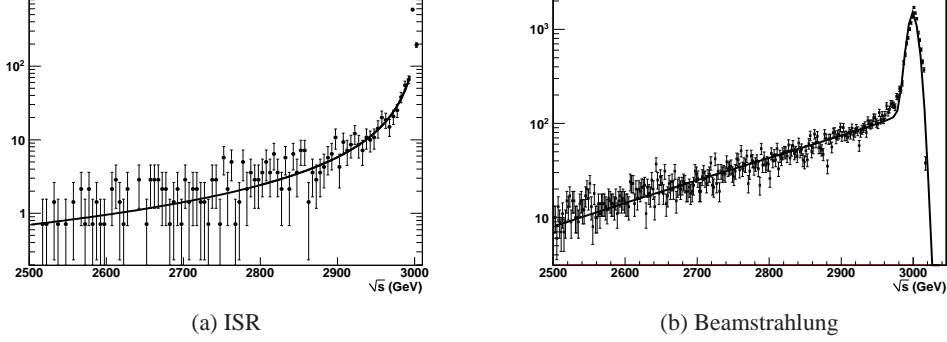


Figure 6: Centre-of-mass energy distribution including (a) ISR and (b) ISR and beamstrahlung. The points represent the simulation and the lines the phenomenological functions used for describing their shape.

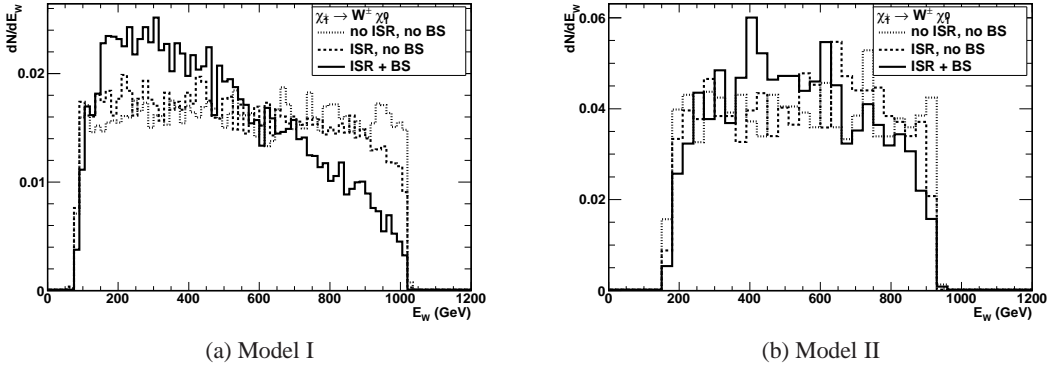


Figure 7:  $W^\pm$  energy spectrum in the  $\chi_1^\pm \rightarrow W^\pm \chi_1^0$  process without radiation effects (dashed), with ISR only (dotted) and with both ISR and beamstrahlung (continuous) for (a) Model I and (b) Model II.

by an approximate solution to the Gribov-Lipatov equation, proposed in [24]. In the formula we leave free the  $\eta$  parameter and the fraction of events off the full energy peak. We determine



them by a fit to the ISR spectrum obtained for PYTHIA signal events (see Figure 6). We study the accuracy on the mass measurements in some of the channels for no radiation effects, ISR only and ISR + BS. Figure 7 shows these effects on the  $W^\pm$  energy spectrum for the  $\chi_1^\pm \rightarrow W^\pm \chi_1^0$  process. In this study we consider only fully hadronic decays of bosons, since we need to reconstruct their energy. The effect of the finite resolution in the determination of the boson energy is included by applying a Gaussian smearing to the energy of the partons produced in the boson decay. The smearing of the energy of the two partons is independent and we test the effect of various energy resolution values in the range  $0 < \delta E/E < 0.125$ . The energy smearing does not account for energy missing in neutrinos. This is particularly important in the reconstruction of  $h^0 \rightarrow b\bar{b}$  decays, where either a  $b$  or a  $c$  hadron decays semi-leptonically.

### 3.3 Analysis and Results

We perform the study by selecting for each of the production and decay processes given above the final state parton topologies and boson contents which have the most favourable signal contribution. We consider only fully hadronic final states and estimate the signal purity and the dominant SUSY background processes at generator level assuming perfect jet clustering and gauge boson identification. The fraction of SUSY final states yielding a 2- $q$  topology is 4.7% (2.3%), a 4- $q$  is 13.3% (1.8%), a 6- $q$  is 3.3% (0.5%) and an 8- $q$  is 4.0% (0.8%) for model I (II), respectively. In model II, the branching fractions of decays into a  $\tilde{\tau}^\pm \rightarrow \tau^\pm \chi_1^0$  are important, which explains the reduced rate of multi-quark final states. However, these modes are not considered here, since our study focuses on decays into bosons.

We assume to operate the collider at 3 TeV for an integrated luminosity of  $2 \text{ ab}^{-1}$  with unpolarised beams. Mass fits are performed on samples of bosons in the selected topology populated with either signal only or inclusive SUSY events and we study the evolution of the statistical accuracy on the masses with the smearing of the energy spectrum due to beam radiation and detector energy resolution effects. We estimate the change in signal purity with the parton energy resolution and the identification of the topology using only reconstructed quantities in section 3.4.

#### 3.3.1 $\chi_1^\pm \rightarrow W^\pm \chi_1^0$

The  $e^+e^- \rightarrow \chi_1^+ \chi_1^- \rightarrow W^+ \chi_1^0 W^- \chi_1^0$ ;  $W \rightarrow q\bar{q}'$  process leads to a distinctive final state with four hadronic jets and missing energy. The SUSY background in model I is almost entirely due to charginos produced through  $e^+e^- \rightarrow e_L^+ e_L^-$ ,  $e_L^\pm \rightarrow \chi_1^\pm \nu_e$ , which account for 12% of the inclusive  $WW$  + missing energy SUSY sample. Since the chargino energy in this process is lower than the beam energy the  $W$  energy is correspondingly shifted to lower values. In the case of model II, the signal  $e^+e^- \rightarrow \chi_1^+ \chi_1^-$  accounts for 87% of the  $W^+W^-$  + missing energy final state with background contributions from  $\chi_2^+ \chi_2^-$  and  $\chi_2^+ \chi_1^- + \text{c.c.}$  The main standard model irreducible background is due to  $e^+e^- \rightarrow W^+W^- \nu_e \bar{\nu}_e$ , which has a cross section of 124 fb. However, the  $W$  production in this process is forward peaked while it is central in SUSY s-channel signal events. Requiring each  $W$  boson to be produced within  $|\cos \theta| < 0.85$ , where  $\theta$  is its polar angle reduces the  $WW\nu\nu$  cross section to 28.7 fb. The energy distribution of  $W^\pm$  bosons in  $WW\nu\nu$  events within the angular acceptance, generated with Comphep 4.5.1 [25], is

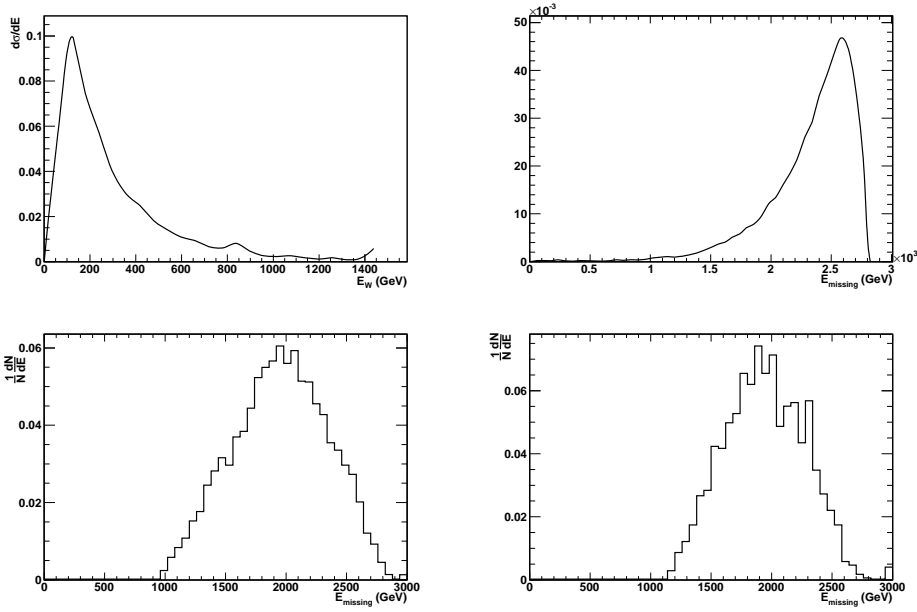


Figure 8: Kinematics of  $e^+e^- \rightarrow W^+W^-v_e\bar{v}_e$  and events with  $|\cos\theta_W| < 0.85$  obtained with Comphep 4.5.1: (upper left)  $W^\pm$  energy spectrum and (upper right) missing energy spectrum. Missing energy distribution for signal  $e^+e^- \rightarrow \chi_1^+\chi_1^-$  events for (lower left) model I and (lower right) model II.

shown in Figure 8. This background affects only the lower endpoint of the  $W$  energy spectrum. Further, the bulk of the signal SUSY events can be separated from this background based on the event missing energy. The results of the 1-par fit of the  $\chi_1^\pm$  mass performed for spectra with no radiation, only ISR and also beamstrahlung effects are given in Table 4. Here, we keep

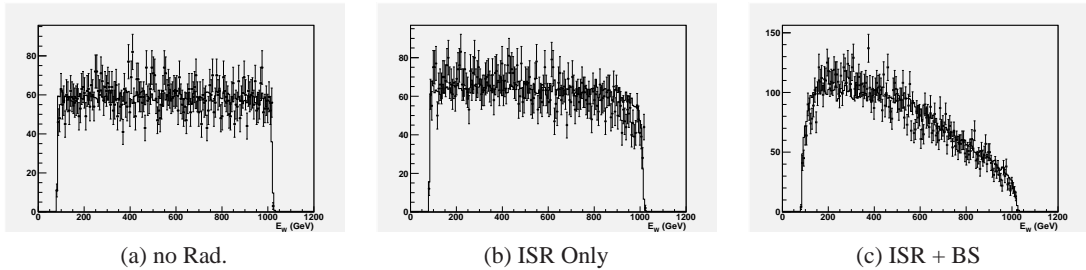


Figure 9:  $W^\pm$  energy spectrum in the four-jet topology,  $2W +$  missing energy final state for  $\chi_1^+\chi_1^-$  signal events in model I at 3 TeV with (a) no radiation. (b) only ISR and (c) ISR+BS. The points with error bars are the simulation and the line the fitted spectrum.

the lightest neutralino mass,  $M_{\chi_1^0}$ , fixed to its model value, since it should be independently determined in the  $e^+e^- \rightarrow \tilde{\mu}_R^+\tilde{\mu}_R^- \rightarrow \mu^+\mu^-\chi_1^0\chi_1^0$  process and the corresponding  $e^+e^- \rightarrow \tilde{e}_R^+\tilde{e}_R^-$

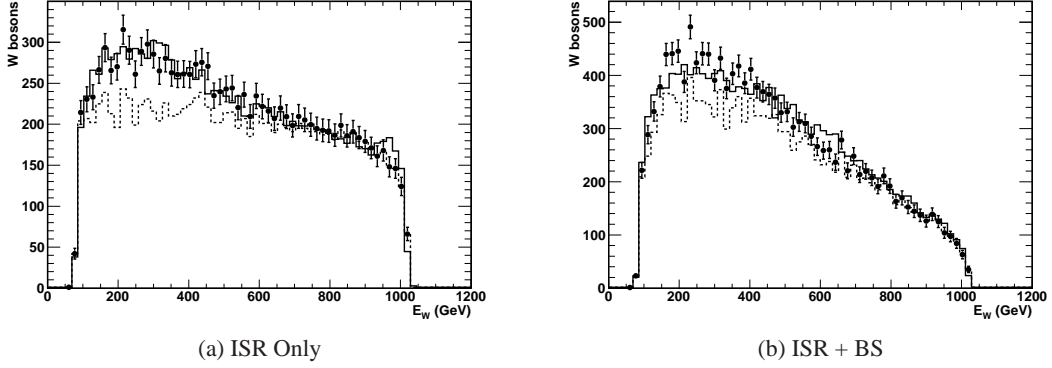


Figure 10:  $W^\pm$  energy spectrum in the four jet topology, 2  $W$  + missing energy final state for inclusive SUSY events in model I at 3 TeV with only ISR (a) and ISR+BS (b). The points with error bars are the simulation, the continuous line the fitted spectrum and the dashed line the fitted contribution from  $\chi_1^+ \chi_1^-$  signal events.

Table 4: Statistical accuracy on  $\chi_1^\pm$  mass from a fit to the  $E_{W^\pm}$  endpoints for  $\chi_1^+ \chi_1^-$  signal events and  $2 \text{ ab}^{-1}$  of integrated luminosity at 3 TeV, under different assumptions

Particle	Mass (GeV)	No Rad	ISR	ISR+BS $\delta E/E=0$	ISR+BS $=0.025$	ISR+BS $=0.05$
Model I $\chi_1^\pm$	643.2	$\pm 0.91$	$\pm 1.39$	$\pm 2.09$	$\pm 2.89$	$\pm 3.60$
Model II $\chi_1^\pm$	1062.2	$\pm 6.10$	$\pm 8.25$	$\pm 10.11$	$\pm 11.0$	$\pm 12.0$

to an accuracy of  $\pm 1.0$  GeV [26]. The fitted spectra are shown in Figure 9. We estimate the systematic uncertainty by varying  $M_{\chi_1^0}$  within this range and repeating the fit, it amounts to  $\pm 2$  GeV on the determination of  $M_{\chi_1^\pm}$ .

The relative mass accuracy for the two models scales with production cross section as expected. We notice that the deterioration of the mass accuracy due to BS is larger for model I (+50.4%), where the  $\chi_1^\pm$  mass is significantly smaller compared to the beam energy, compared to model II (+28.4%), since the  $\chi_1^+ \chi_1^-$  threshold sits close to  $\sqrt{s}$  and the BS effects are dumped by the fall of the production cross section near threshold. Then, we repeat the fit accounting for both the direct chargino production contribution to the  $W$  energy spectrum and that from  $\tilde{e}_L^\pm \rightarrow \chi^\pm \nu_e$  decays. These decays still offer some sensitivity to the chargino mass but cannot be distinguished from chargino pair production in the event selection. At this specific benchmark point the selectron left mass  $M_{e_L}$  cannot be measured with the electron energy spectrum in the  $e^+ \chi_1^0 e^- \chi_1^0$  final state since the spectrum is dominated by the  $\tilde{e}_R \tilde{e}_R$  process. It could be measured using the mixed  $e^+ \chi_1^0 h^0 \chi_1^0 h^0$  and possibly  $e^\pm \chi_1^0 W^\mp \nu \chi_1^0$  modes at 3 TeV and in a threshold scan.

Table 5: Statistical accuracy on  $\chi_1^\pm$  mass from a fit to the  $E_{W^\pm}$  endpoints for 2  $W$  + missing energy inclusive SUSY events and 2  $\text{ab}^{-1}$  of integrated luminosity at 3 TeV, under different assumptions

Particle	Mass (GeV)	No Rad	ISR	ISR+BS $\delta E/E=0$	ISR+BS =0.025	ISR+BS =0.050
Model I						
2-par Fit $\chi_1^\pm$	643.2	$\pm 1.4$	$\pm 1.7$	$\pm 2.6$	$\pm 3.8$	$\pm 4.1$
3-par Fit $\chi_1^\pm$	643.2	$\pm 2.0$	$\pm 2.3$	$\pm 3.5$	$\pm 4.8$	$\pm 5.2$
$\tilde{e}_L$	1102.2	$\pm 48$	$\pm 50$	$\pm 56$	$\pm 63$	$\pm 66$

We perform fits where  $M_{\tilde{e}_L}$  is either kept at its model value or it is treated as a free parameter, while the  $\chi_1^\pm$  mass and the relative contribution of the two processes to the  $W$  spectrum are kept free. Results are summarised in Table 5 and Figure 10.

### 3.3.2 $\chi_2^0 \rightarrow h^0 \chi_1^0$

The  $\chi_2^0 \rightarrow h^0 \chi_1^0$  decay of the chargino pair yields two Higgs bosons plus missing energy. The same final states originates also from  $e^+e^- \rightarrow \tilde{\nu}_\ell \tilde{\nu}_\ell \rightarrow \chi_2^0 \nu_\ell \chi_2^0 \nu_\ell$ . For the parameters of model I  $M_{\tilde{\nu}_\ell} = 1097.2$  GeV, the  $e^+e^- \rightarrow \tilde{\nu}_\ell \tilde{\nu}_\ell$  production cross section is 14.5 fb. The sneutrino channel

Table 6: Statistical accuracy on  $\chi_2^0$  mass from a fit to the  $E_{h^0}$  endpoints for  $\chi_2^0 \chi_2^0$  signal events and 2  $\text{ab}^{-1}$  of integrated luminosity at 3 TeV, under different assumptions

Particle	Mass (GeV)	No Rad	ISR	ISR+BS $\delta E/E=0$	ISR+BS =0.025	ISR+BS =0.05
Model I $\chi_2^0$	643.2	$\pm 1.01$	$\pm 1.17$	$\pm 2.58$	$\pm 3.59$	$\pm 4.54$
Model II $\chi_2^0$	1064.2	$\pm 10.64$	$\pm 11.12$	$\pm 16.71$	$\pm 19.04$	$\pm 23.42$

accounts for 68% of the 4-jet,  $hh$  + missing energy inclusive SUSY sample. In model II, the tree-level sneutrino production cross section is 6 fb which drops to 2.3 fb accounting for ISR and BS and the signal purity is 89%. This final state is expected to be virtually immune from irreducible SM backgrounds, since the cross section for double WW fusion light Higgs production,  $e^+e^- \rightarrow h^0 h^0 \nu_e \bar{\nu}_e$  is only  $\simeq 1$  fb for  $115 < M_h < 130$  GeV [27]. Fit results on signal events are summarised in Table 6 and the fitted spectra given in Figure 11. Again, the relative increase of the statistical uncertainty due to BS is larger for model I compared to model II. We repeat the

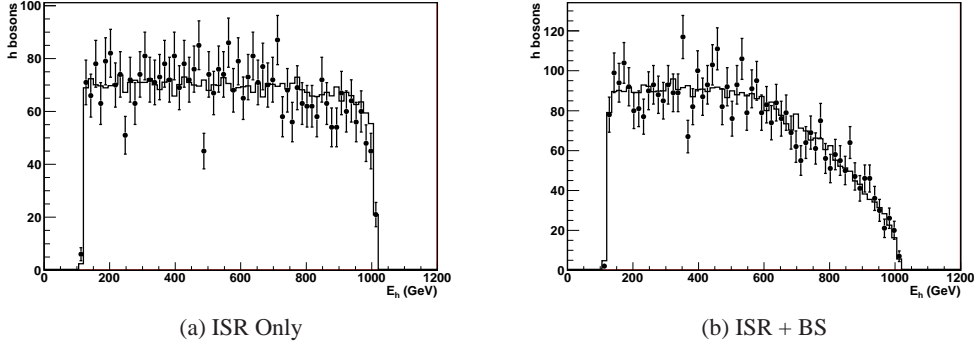


Figure 11:  $h^0$  energy spectrum in the 4-jet,  $2h +$  missing energy final state for  $\chi_2^0 \chi_2^0$  signal events in model I at 3 TeV with only ISR (left) and ISR+BS (right). The points with error bars are the simulation and the continuous line the fitted spectrum.

Table 7: Statistical accuracy on  $\chi_2^0$  mass from a fit to the  $E_{W^\pm}$  endpoints for  $2h +$  missing energy inclusive SUSY events and  $2 \text{ ab}^{-1}$  of integrated luminosity at 3 TeV, under different assumptions

Particle	Mass (GeV)	No Rad	ISR	ISR+BS $\delta E/E=0$	ISR+BS $=0.025$	ISR+BS $=0.050$
Model I						
$\chi_2^0$	643.2	$\pm 2.5$	$\pm 3.2$	$\pm 5.3$	$\pm 6.8$	$\pm 8.4$
$\tilde{\nu}_\ell$	1097.2	$\pm 43.4$	$\pm 51.8$	$\pm 52.7$	$\pm 60.4$	$\pm 69.3$

fit accounting for both the direct  $\chi_2^0$  production and the irreducible  $\tilde{\nu}_\ell$  SUSY background contribution to the  $W$  energy spectrum for model I where its contribution is more important. Since the sneutrino decays through a  $\chi_2^0$ , the  $h^0$  energy spectrum retains some sensitivity to the  $\chi_2^0$  mass. A multi-parameter fit with the  $\chi_2^0$  and  $\tilde{\nu}_\ell$  masses treated as free parameters, together with the relative contribution of the two processes to the  $h^0$  spectrum is performed (see Figure 12). Results are summarised in Table 7.

### 3.3.3 $\chi_2^\pm \rightarrow W^\pm \chi_1^0$ , $\chi_2^\pm \rightarrow W^\pm \chi_2^0$ , $\chi_2^\pm \rightarrow h^0 \chi_1^\pm$

The  $\chi_2^\pm$  chargino has one of largest production cross section for supersymmetric particles. Contrary to the lighter states discussed above, there is no dominant decay channel and the analysis has to include several final states. We consider here  $W^\pm$ ,  $Z^0$  and  $h^0$  spectra from combinations of decays with both 6- and 8-parton final states. The channels we have considered are not exhaustive but are representatives of the topologies offered by decays of  $\chi_2^+ \chi_2^-$  pairs. The 6-jet topology accounts for 31% of the total yield of  $\chi_2^+ \chi_2^-$  pairs. The  $W^+ W^- h^0 +$  missing energy final state receives two contributions from signal  $\chi_2^+ \chi_2^-$  pair production:

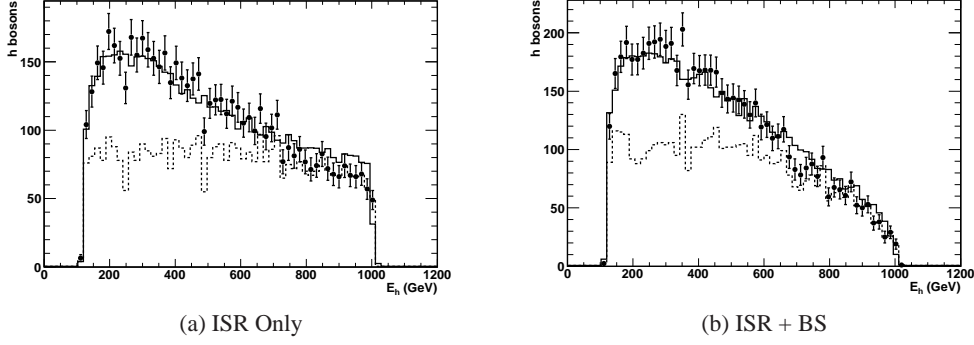


Figure 12:  $h^0$  energy spectrum in the 4-jet, 2  $h$  + missing energy final state for inclusive SUSY events in model I at 3 TeV with only ISR (left) and ISR+BS (right). The points with error bars are the simulation, the continuous line the fitted spectrum and the dashed line the fitted contribution from  $\chi_2^0 \chi_2^0$  events.

Table 8: Statistical accuracy on  $\chi_2^\pm$  mass from the combination of fits to the  $E_{W^\pm}$  and  $E_{h^0}$  spectra for  $\chi_2^+ \chi_2^-$  signal events in 6-jet  $WW h$  and 8-jet  $WW Zh$  topologies and  $2 \text{ ab}^{-1}$  of integrated luminosity at 3 TeV, under different assumptions

Particle	Mass (GeV)	No Rad	ISR	ISR+BS	ISR+BS	ISR+BS
				$\delta E/E=0$	$=0.025$	$=0.050$
Model I						
$\chi_2^\pm$	916.7	$\pm 2.2$	$\pm 2.8$	$\pm 3.6$	$\pm 3.9$	$\pm 4.2$

$e^+e^- \rightarrow \chi_2^+ \chi_2^+ \rightarrow W^+ \chi_2^0 W^- \chi_1^0 \rightarrow W^+ h^0 \chi_1^0 W^- \chi_1^0$  with  $h \rightarrow b\bar{b}$ ,  $W \rightarrow q\bar{q}'$  and  $e^+e^- \rightarrow \chi_2^+ \chi_2^+ \rightarrow h^0 \chi_1^+ W^- \chi_1^0 \rightarrow h^0 W^+ \chi_1^0 W^- \chi_1^0$  with  $h \rightarrow b\bar{b}$ ,  $W \rightarrow q\bar{q}'$ . Each event has two  $W$  and one Higgs boson. The purity in  $\chi_2^+ \chi_2^-$  pairs is 77 % with other SUSY contribution to this final state coming from  $\chi_3^0 \chi_4^0$  and  $\chi_1^\pm \chi_2^\mp$ . The  $W$  spectrum combines  $W$ s produced in the direct  $\chi_2^\pm$  decay into two different states,  $\chi_2^0$  and  $\chi_1^0$ . In the final state also the Higgs boson is sensitive to the  $\chi_2^\pm$  mass, through the contribution from the  $\chi_2^\pm \rightarrow h^0 \chi_1^\pm$  decays, while part of the bosons come from the  $\chi_2^0$  decay. In both cases we perform a 2-par fit leaving both the  $M_{\chi_2^\pm}$  and the fraction of the two contributions free (see Figure 13). Then, we consider processes with four bosons yielding the 8-jet topology, which accounts for 19% of the  $\chi_2^+ \chi_2^-$  final states. The  $Z^0 h^0 W^+ W^-$  final state has 85% contribution from  $\chi_2^+ \chi_2^-$  pairs with the remaining mostly due to  $\chi_3^0 \chi_4^0$ . We use both the  $Z^0$  and the  $h^0$  spectrum to perform the mass fits. In this topology the  $Z^0$  energy spectrum from the process  $e^+e^- \rightarrow \chi_2^+ \chi_2^- \rightarrow Z^0 \chi_1^+ W^- \chi_2^0 \rightarrow Z^0 W^+ W^- h^0 \chi_1^0 \chi_1^0$  receives almost exclusively contributions from the direct  $\chi_2^\pm \rightarrow Z^0 \chi_1^\pm$  decay. For the fit to the  $h^0$  spectrum we include the contribution from the  $\chi_2^\pm \rightarrow h^0 \chi_1^\pm$  and that from  $\chi_2^0 \rightarrow h^0 \chi_1^0$ , leaving the contribution of the two processes free, as done for the 6-jet topology (see Figure 13). Results are combined and the statistical uncertainties are summarised in Table 8.

### 3.3.4 $\chi_{3,4}^0 \rightarrow W^\pm \chi_1^\mp$

The  $e^+e^- \rightarrow \chi_3^0 \chi_4^0$  process has a sizable cross section in model I and a good number of signal events can be reconstructed. The decay channel considered here is  $\chi_{3,4}^0 \rightarrow W^\pm \chi_1^\mp \rightarrow W^\pm W^\mp \chi_1^0$  which gives an 8-jet topology with, 4  $W$  bosons and missing energy. This final state is challenging, due to its large jet multiplicity, but the signature is striking and there are essentially no SUSY or SM irreducible background processes contributing to it. In each event two of the  $W$  are sensitive to the  $\chi_{3,4}^0$  mass and the others to the  $\chi_1^\pm$  mass. Since this can be precisely measured in the 2  $W$  + missing energy channel, it is safe to assume here that its mass is known. Results are given in Table 9 and Figure 14. The structure of the cMSSM implies that the two heaviest neutralinos,  $\chi_3^0$  and  $\chi_4^0$  are nearly degenerate. However, this is not a general feature of supersymmetry and it does not apply to less constrained scenarios, such as the MSSM, where the  $\chi_4^0$  -  $\chi_3^0$  mass splitting can be  $\sim 20\%$  of their masses, or larger. Therefore, we repeat the fit, leaving the masses of  $\chi_3^0$  and  $\chi_4^0$  free and test the result for a mass splitting of 10 GeV, as in our model I, and one of 40 GeV obtained by decreasing the  $\chi_3^0$  mass. We find a resolution on the  $\chi_3^0$  -  $\chi_4^0$  mass splitting of  $\sim 15$ -18 GeV and masses which are apart  $\sim 35$  GeV and more can be resolved.

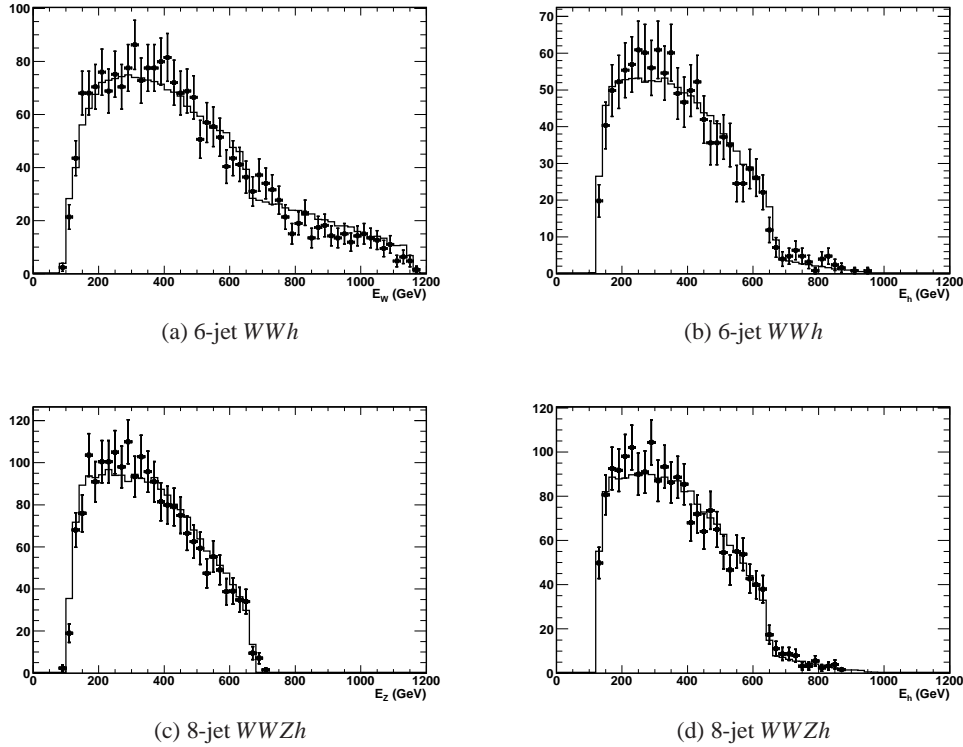


Figure 13: Energy spectra for  $\chi_2^+ \chi_2^-$  signal events: (upper row) in the six jet  $WWh$  final state and (lower row) in the eight jet  $WWZh$  final state with ISR and BS effects for model I at 3 TeV. The points with error bars are the simulation and the line the fitted spectrum.

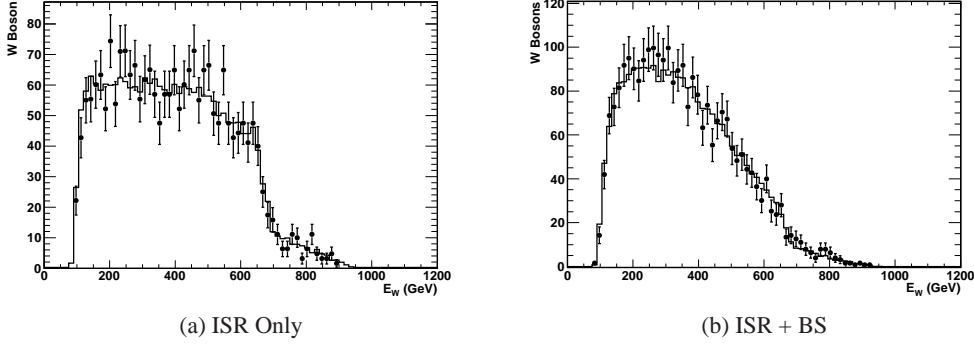


Figure 14:  $W^\pm$  energy spectrum in the 8-jet topology, 4  $W$  + missing energy final state at 3 TeV with only ISR (left) and ISR+BS (right) for  $\chi_3^0\chi_4^0$  signal events in model I. The points with error bars are the simulation and the line the fitted spectrum.

Table 9: Statistical accuracy on  $\chi_{3,4}^0$  mass from a fit to the  $E_{W^\pm}$  endpoints for  $\chi_3^0\chi_4^0$  signal events and  $2 \text{ ab}^{-1}$  of integrated luminosity at 3 TeV, under different assumptions

Particle	Mass (GeV)	No Rad	ISR	ISR+BS $\delta E/E=0$	ISR+BS $=0.05$
Model I					
$\chi_3^0$	905.5	$\pm 7.1$	$\pm 7.9$	$\pm 12.6$	$\pm 15.1$
$\chi_4^0$	916.7	$\pm 8.7$	$\pm 8.9$	$\pm 13.0$	$\pm 15.4$

### 3.4 Energy Resolution Effects

The effect of the jet energy resolution on the  $\chi_1^\pm$  masses for both models are shown in Figure 15 in terms of the relative change of the statistical accuracy of the mass determination as a function of the parton energy resolution  $\delta E/E$ . As expected, the effect is larger when beam radiation is not considered. We establish a quantitative criterion for the energy resolution requiring that the contribution from the parton energy resolution to the statistical mass accuracy should not exceed the combined effect of ISR and beamstrahlung. We assume that these contributions adds quadratically and derive the limits to  $\delta E/E$  for the different channels which are summarised in Figure 16. Then, we consider the effect of the parton energy resolution on the di-jet invariant mass. We study the specific case of the  $Z^0$  identification in the 8-jet  $e^+e^- \rightarrow \chi_2^+\chi_2^+ \rightarrow Z^0\chi_1^+W^-\chi_1^0 \rightarrow Z^0W^+\chi_1^0W^-\chi_1^0$ ;  $Z \rightarrow q\bar{q}$ ,  $W \rightarrow q\bar{q}'$  process, which is the process most sensitive to di-jet mass resolution in model I, due to the large  $W$  yield. We identify the  $Z^0$  boson requiring that the di-jet mass is compatible with the nominal mass,  $M_Z=91.2 \text{ GeV}$ , within  $3 \sigma_Z$ , where  $\sigma_Z$  is the peak Gaussian width measured on genuine  $Z^0 \rightarrow q\bar{q}$  di-jets. We vary the Gaussian parton energy resolution (see Figure 17) and study the purity in real  $Z^0$  bosons selected by this selection. Since  $W^\pm$  bosons are dominant in 8-jet topology SUSY events (53%) and  $Z^0$  bosons



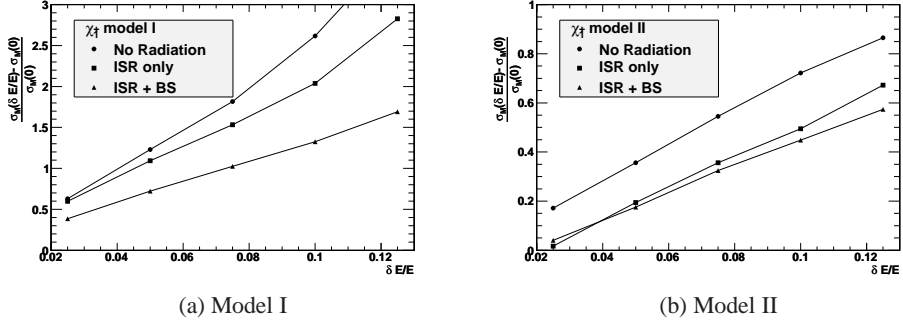


Figure 15: Relative change of the statistical accuracy on the  $\chi_1^\pm$  mass as a function of the jet energy resolution from one-parameter  $\chi^2$  fits to the energy spectrum for signal events in model I (a) and II (b).

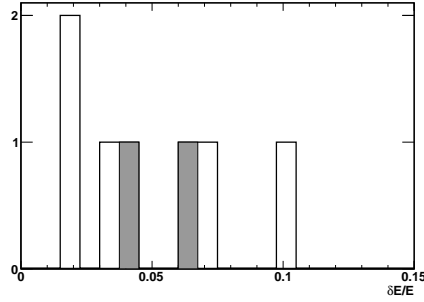


Figure 16: Values of the relative energy resolution  $\delta E/E$  at which its contribution on the mass statistical uncertainties equals that of ISR and beamstrahlung for the channels considered in this study. Model I is shown by the open histogram and model II by the grey histogram.

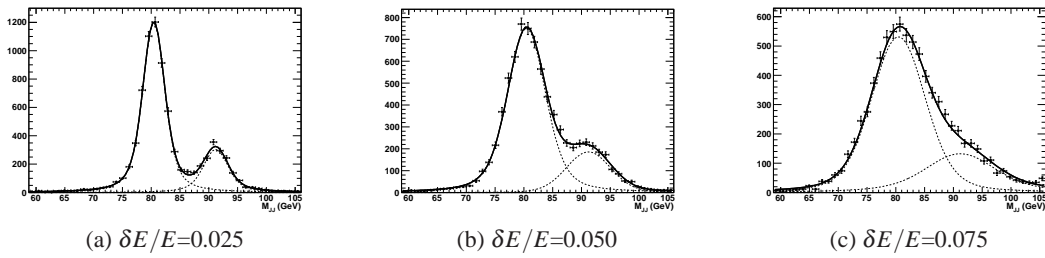


Figure 17: Di-jet invariant mass in 8-jet inclusive SUSY events in model I for various values of parton energy resolution.

Table 10: Gaussian width of the  $Z^0$  peak and purity of  $Z^0$  decays selected from their compatibility with the  $Z^0$  mass in 8-jet inclusive SUSY events in model I for various values of parton energy resolution.

$\delta E/E$	$\sigma_Z$ (GeV)	Purity
0.	1.64	0.877
0.025	2.42	0.720
0.040	3.33	0.418
0.050	4.14	0.290
0.075	5.34	0.220

make only 15.5% of the di-jets, the leakage from the  $W^\pm$  peak is important already for moderate values of the energy resolution, as shown in Table 10.

Operating the collider with polarised beams may be important to improve the statistical accuracy in the determination of heavier states such as  $\chi_3^0$  and  $\chi_4^0$ . However, given the broad scope of the research program at a multi-TeV collider various states of polarisation will be likely selected, making our assumption a fair estimate for the total cumulative statistics of signal events.

### 3.4.1 Validation with Full Simulation and Reconstruction

In order to validate the results obtained above at generator level, accounting only for a simple energy smearing, the  $\chi_1^+ \chi_1^-$  and  $\chi_2^0 \chi_2^0$  analyses are repeated on fully simulated and reconstructed events to verify the accuracy when accounting for the reconstruction effects in full.

A sample of inclusive SUSY events for model I, generated with ISR+BS, corresponding to  $0.5 \text{ ab}^{-1}$  of integrated luminosity, is fully simulated and reconstructed using the CLIC version of the ILD detector concept. First, the 4-jet + missing energy events are reconstructed. Events are pre-selected requiring a visible energy  $250 < E_{tot} < 1800 \text{ GeV}$ , an energy in charged particles larger than 150 GeV, transverse energy larger than 200 GeV, a jet multiplicity  $2 \leq N_{jets} < 5$  and at least 20 charged reconstructed particles. Jets clustering is performed using the Durham jet algorithm [28], with  $y_{cut} = 0.0025$ , on the reconstructed particle flow objects of the Pandora particle flow package [29]. These events are then forced into four jets and the di-jet invariant mass for all the three possible pairings is computed. The jet pairing minimising the difference between the di-jet invariant masses is selected, provided the mass difference is below 20 GeV. The resulting mass distribution on generated SUSY di-boson events is shown in Figure 18. The fraction of  $W^+W^-$ ,  $Z^0Z^0$  and  $h^0h^0$  events is extracted by a  $\chi^2$  fit to the di-jet mass distribution. The  $W^\pm$  and  $Z^0$  mass peaks are parametrised as Breit-Wigner functions convoluted with a Gaussian term describing the experimental resolution. The mass and width values of the Breit-Wigner functions are fixed to their generated values, while the total area and the width of the Gaussian resolution terms are left free in the fit. The  $h^0$  peak, which has negligible natural width, is modelled as the sum of two Gaussian curves, one representing the correctly reconstructed signal events, centred at the nominal  $M_h$  value, the second describing decays where the mass has a lower reconstructed

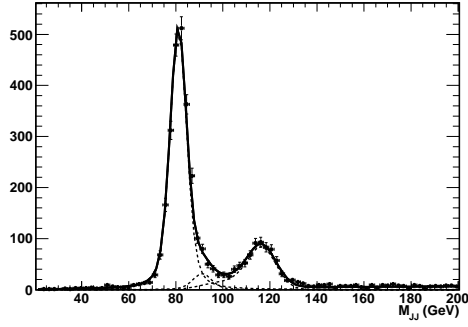


Figure 18: Di-jet invariant mass for di-boson inclusive SUSY fully simulated and reconstructed events for model I with the fitted contributions from  $W^\pm$ ,  $Z^0$  and  $h^0$

Table 11: Fraction of  $W^\pm$ ,  $Z^0$  and  $h^0$  bosons from the fit to the di-jet invariant mass distribution in 4-jet + missing energy inclusive SUSY events for model I for  $0.5 \text{ ab}^{-1}$  of integrated luminosity, compared to the generated values.

Boson	Fitted	Simulated
	Fraction of Evt.	Fraction of Evt.
$W^\pm$	$0.650 \pm 0.011$	$0.645 \pm 0.005$
$Z^0$	$0.040 \pm 0.009$	$0.020 \pm 0.002$
$h^0$	$0.215 \pm 0.010$	$0.243 \pm 0.003$

value due to semi-leptonic  $b$  decays. The central value, width and fraction of events in this second Gaussian is extracted by a fit to a pure sample of decays into  $h^0$  bosons and fixed in the fit, while the Gaussian width of the main peak is kept free. Results are given in Table 11 and the fitted functions are overlaid to the reconstructed spectrum in Figure 18.

Then, events with di-jets compatible with the  $WW$  hypothesis are selected. The total selection efficiency is 60% for  $\chi_1^+ \chi_1^- \rightarrow W^+ \chi_1^0 W^- \chi_1^0 \rightarrow q\bar{q}' \chi_1^0 q\bar{q}' \chi_1^0$  signal events. This efficiency is independent on the  $W$  energy and the reconstruction and selection criteria do not introduce any significant bias to this distribution (see Figure 19). The sample of selected 4-jet  $WW$  candidate events has a purity of 86% and consists of 78% signal  $\chi_1^+ \chi_1^- \rightarrow W^+ \chi_1^0 W^- \chi_1^0$ , 7.5%  $\tilde{e}_L^+ \tilde{e}_L^- \rightarrow \chi_1^+ \chi_1^- \nu_e \bar{\nu}_e$  and 0.2% of other 4-jet  $WW$  SUSY processes (see the left panel of Figure 20). The fraction of background fake- $WW$  events is obtained from the fit to the di-jet invariant mass distribution and the shape of their di-jet energy spectrum directly extracted from the reconstructed events, using the di-jet mass side-bands  $40 < E_{jj} < 60 \text{ GeV}$  and  $140 < E_{jj} < 160 \text{ GeV}$ , and subtracted.

The multi-parameter fit to the  $\chi_1^\pm$  and  $\tilde{e}_L$  masses is repeated on the background-subtracted  $W^\pm$  energy distribution of selected fully simulated and reconstructed events (see Figure 21). The result is  $M_{\chi_1^\pm} = (643 \pm 14) \text{ GeV}$  and  $M_{\tilde{e}_L^\pm} = (1100 \pm 104) \text{ GeV}$ , where the statistical accuracies

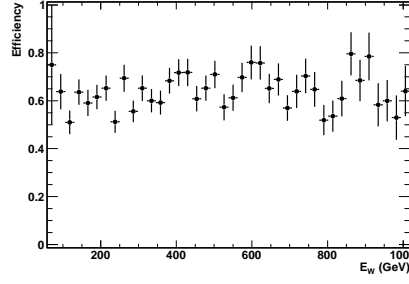


Figure 19: Efficiency for event reconstruction and selection on fully simulated and reconstructed 4-jet  $\chi_1^+ \chi_1^- \rightarrow W^+ \chi_1^0 W^- \chi_1^0 \rightarrow q\bar{q}' \chi_1^0 q\bar{q}' \chi_1^0$  signal events as a function of the  $W$  energy.

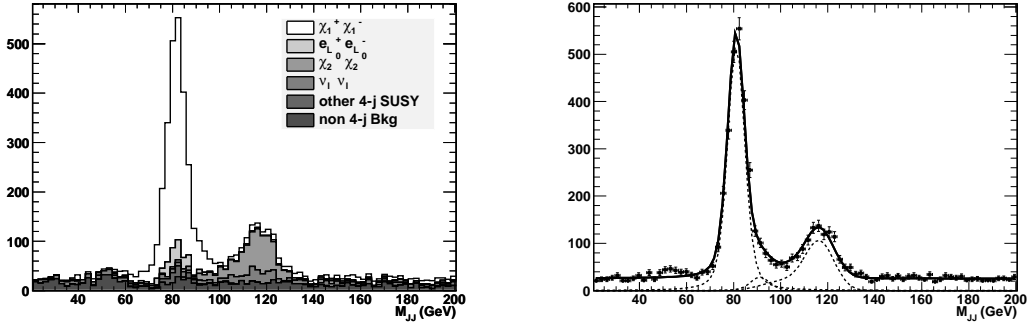


Figure 20: Di-jet invariant mass for selected inclusive SUSY fully simulated and reconstructed events for model I (left) with the different sources highlighted and (right) with the background and signal components fitted.

are consistent to those obtained on a smeared simulated spectrum of equal statistics,  $M_{\chi_1^\pm} = (643 \pm 12)$  GeV and  $M_{\tilde{e}_L^\pm} = (1100 \pm 110)$  GeV. Finally, we select events with di-jets compatible with the  $hh$  hypothesis. The total selection efficiency is 69% for  $\chi_2^0 \chi_2^0 \rightarrow h^0 \chi_1^0 h^0 \chi_1^0 \rightarrow b\bar{b} \chi_1^0 b\bar{b} \chi_1^0$ . The multi-parameter fit to the  $\chi_2^0$  and  $\tilde{\nu}_\ell$  masses is repeated on the background-subtracted  $h^0$  energy distribution of selected fully simulated and reconstructed events (see Figure 22). The result is  $M_{\chi_2^0} = (643 \pm 26)$  GeV and  $M_{\tilde{\nu}_\ell} = (1097 \pm 148)$  GeV, where the statistical accuracies are consistent to those obtained on a smeared simulated spectrum of equal statistics,  $M_{\chi_2^0} = (643 \pm 21)$  GeV and  $M_{\tilde{\nu}_\ell} = (1097 \pm 123)$  GeV. The degradation of the statistical accuracy in the analysis of the fully simulated and reconstructed data compared to that on the smeared generator-level events, is likely due to the larger background from fake 4-jet  $hh$  events, which is not included at generator level. In this study we do not consider jet flavour tagging for consistency with the simple procedure adopt for the generator level study. However, by applying  $b$ -tagging to the four jets, the background, which does not contain two light Higgs bosons, can be largely reduced.

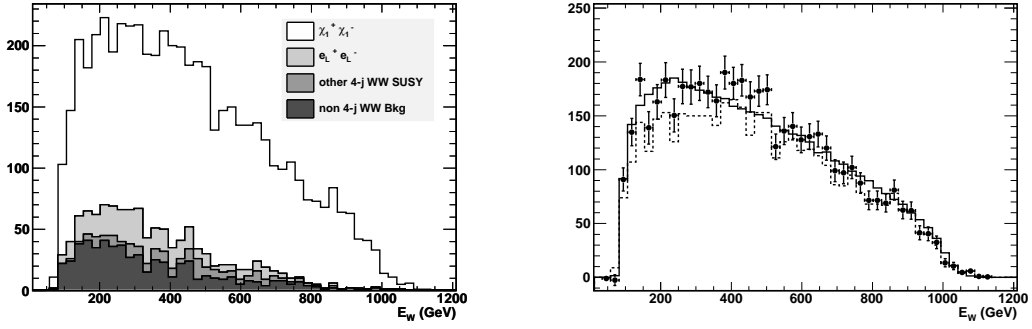


Figure 21: Fits of fully simulated and reconstructed events in model I: (left)  $W^\pm$  energy spectrum of selected 4-jet  $WW$  candidate events energy spectrum and (right) background subtracted spectrum (points with error bars) with the result of the 3-par fit (continuous line).

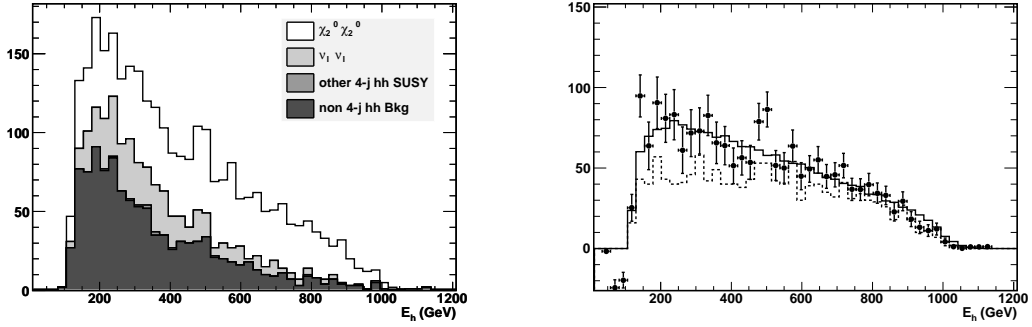


Figure 22: Fits of fully simulated and reconstructed events in model I: (left)  $h^0$  energy spectrum of selected 4-jet  $hh$  candidate events energy spectrum and (right) background subtracted spectrum (points with error bars) with the result of the 3-par fit (continuous line).

In conclusion, the analysis of fully simulated and reconstructed SUSY events where 4-jet,  $WW$  and  $hh$  candidates are selected based on the reconstructed topology and di-jet invariant mass shows that reconstruction efficiencies are quite large and flat with the boson energy. Backgrounds from other final states can be reliably estimated and subtracted in a model-independent way. The statistical accuracies obtained on the extraction of gaugino and slepton masses from these data are found to be comparable to those from the smeared generator, once the reconstruction efficiencies are taken into account.

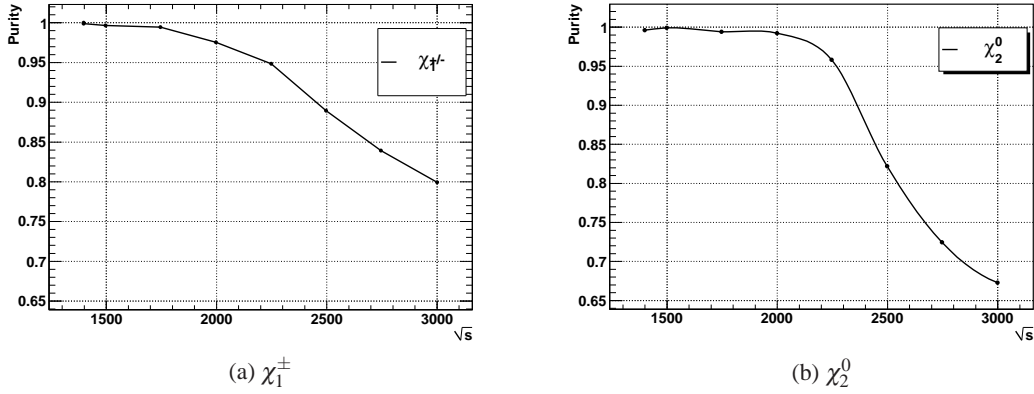


Figure 23: Purity for the  $\chi_1^+ \chi_1^-$  and  $\chi_2^0 \chi_2^0$  process in 4-jet final state as a function of the  $\sqrt{s}$  energy.

## 4 Mass Determination by Threshold Energy Scans

An  $e^+e^-$  linear collider with tunable beam energy can determine the sparticle masses by performing energy scans of their pair production cross section near threshold. In principle, this method provides a better mass accuracy, compared to the kinematic end-point method discussed above. Threshold energy scans put significant requirements on the machine performance and versatility. Not only the beam energy needs to be varied over a broad range, but, since the cross section at threshold is small, a large luminosity must be preserved in lower energy operation. Beamstrahlung effects are important at threshold, while SUSY background are reduced, at least for the lighter states. We study the processes

- $e^+e^- \rightarrow \chi_1^+ \chi_1^- \rightarrow W^+ \chi_1^0 W^- \chi_1^0; W \rightarrow q\bar{q}'$ ,
- $e^+e^- \rightarrow \chi_2^0 \chi_2^0 \rightarrow h^0 \chi_1^0 h^0 \chi_1^0; h \rightarrow b\bar{b}$ ,
- $e^+e^- \rightarrow \chi_2^+ \chi_2^+ \rightarrow W^+ \chi_2^0 W^- \chi_1^0 \rightarrow W^+ h^0 \chi_1^0 W^- \chi_1^0; h \rightarrow b\bar{b}, W \rightarrow q\bar{q}'$
- $e^+e^- \rightarrow \chi_2^+ \chi_2^+ \rightarrow h^0 \chi_1^+ W^- \chi_1^0 \rightarrow h^0 W^+ \chi_1^0 W^- \chi_1^0; h \rightarrow b\bar{b}, W \rightarrow q\bar{q}'$

for model I. For model II we study

- $e^+e^- \rightarrow \chi_1^+ \chi_1^- \rightarrow W^+ \chi_1^0 W^- \chi_1^0; W \rightarrow q\bar{q}'$

We assume a total integrated luminosity of  $3 \text{ ab}^{-1}$ , where the  $2 \text{ ab}^{-1}$  taken at the maximum energy, as assumed above, are supplemented by  $1 \text{ ab}^{-1}$  of statistics dedicated to the scan of sparticle pair production thresholds at lower energies. At, or below,  $\sqrt{s} = 2 \text{ TeV}$ , the  $\chi_1^+ \chi_1^-$  and  $\chi_2^0 \chi_2^0$  pair production saturates the final states with 4-jet and  $WW$  or  $hh$ , respectively, since slepton production is below threshold due to the larger  $\tilde{e}_L$  and  $\tilde{\nu}_\ell$  masses, as shown in Figure 23. A 1-par  $\chi^2$  fit to the cross section values at the chosen operating energies is performed to extract

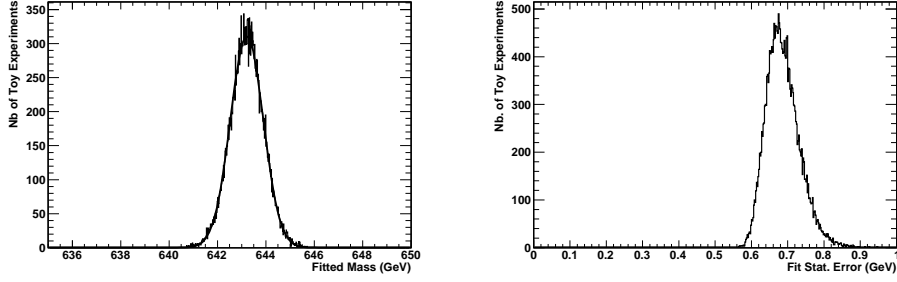


Figure 24: Toy test validation of the threshold scan fit results for  $\chi_1^\pm$  for model I. The corresponding  $\chi^2$  fit result is  $(643.2 \pm 0.68)$  GeV.

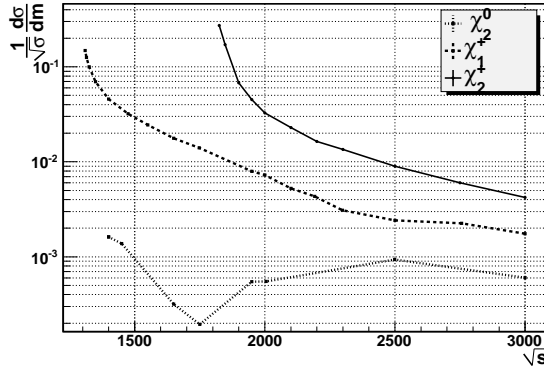


Figure 25: Sensitivity  $\frac{1}{\sqrt{\sigma}} \frac{d\sigma}{dm}$  to sparticle masses in the threshold scan as a function of  $\sqrt{s}$  for model I.

the mass value. The mass and its uncertainty are obtained by assuming a given number of cross section measurements of the relevant pair production process at the  $\sqrt{s}$  values for the scan points. The cross section is computed both at Born level and also adding ISR and beamstrahlung effects using Pythia. The fit results are validated using toy tests. In these we repeat the fits by varying the cross section within its statistical uncertainty at each  $\sqrt{s}$  value and we plot the result. We verify that the result is centred on the simulated mass and its width is consistent with the  $\chi^2$  fit uncertainty (see Figure 24). In order to define a suitable scan strategy, we first study the sensitivity to the sparticle masses as a function of  $\sqrt{s}$ . The sensitivity is defined as  $1/\sqrt{\sigma} d\sigma/dm$ , where  $\sigma$  is the pair production cross section and  $m$  the mass, as in ref. [30]. We compute the cross section  $\sigma$  at various  $\sqrt{s}$  values for a set of closely spaced masses and obtain the derivative  $d\sigma/dm$  of the change of the cross section at each energy per unit of mass change. Results are shown in Figure 25, which indicate that the maximum of the sensitivity to the mass is achieved near threshold. The number of scan points and the share of the statistics among them is optimised by studying the mass uncertainty obtained from the fit for different assumptions.

Table 12: Statistical accuracy on sparticle masses from energy scans under different assumptions for  $2 \text{ ab}^{-1}$  of integrated luminosity at 3 TeV and  $1 \text{ ab}^{-1}$  at two energies near threshold.

Particle	Mass (GeV)	Born	ISR	ISR+BS	ISR+BS +Bkg	w/ Pol (+0.8/0)	w/ Pol (+0.8/-0.6)
Model I							
$\chi_1^\pm$	643.2	$\pm 0.6$	$\pm 0.6$	$\pm 0.7$	$\pm 0.7$	$\pm 0.5$	$\pm 0.4$
$\chi_2^0$	643.1	$\pm 4.3$	$\pm 13.8$	$\pm 24.1$	$\pm 25.6$	$\pm 23.9$	$\pm 18.1$
$\chi_2^\pm$	916.7	$\pm 0.8$	$\pm 0.9$	$\pm 1.3$	$\pm 1.4$	$\pm 1.1$	$\pm 0.9$
Model II							
$\chi_1^\pm$	1062.2	$\pm 6.2$	$\pm 6.4$	$\pm 6.9$		$\pm 5.1$	$\pm 2.8$

We find that it is preferable to concentrate the luminosity in a small number of scan points. For example, the statistical accuracy on the mass of the  $\chi_1^\pm$  in the model I varies from  $\pm 0.85 \text{ GeV}$ , obtained for a four-point scan ( $1310 \leq \sqrt{s} \leq 1950 \text{ GeV}$ ), to  $\pm 0.45 \text{ GeV}$ , when the luminosity is split between just two points, one of which at the peak of the sensitivity ( $\sqrt{s}=1350 \text{ GeV}$ ) and the second close to threshold ( $\sqrt{s}=1310 \text{ GeV}$ ). This confirms the findings of [30] for lower sparticle masses and different luminosity spectrum. Finally, we consider the option of operating the collider with polarised beams. Results are summarised in Table 12. In all cases, except the  $\chi_2^\pm$ , the mass accuracies obtained with a dedicated threshold scan improve on those resulting from the kinematic edge analysis at 3 TeV by factors of 2 or more. The use of polarised beam further improves these accuracies, effectively compensating for the loss of sensitivity due to ISR and BS.

## 5 Conclusions

The determination of chargino and neutralino masses in high-mass SUSY scenarios with two-body decays into  $W^\pm$ ,  $Z^0$  and  $h^0$  bosons provides us with a mean to quantify the effect of radiation, by ISR and beamstrahlung, and parton energy resolution on the accuracy achievable in supersymmetric particle mass measurements at a multi-TeV  $e^+e^-$  linear collider. In our analysis both fits to boson energy spectra and threshold scans are considered for fully hadronic final states. Results from generator-level quantities are validated using fully simulated and reconstructed events in the  $W^+W^- + E_{\text{missing}}$  and  $h^0h^0 + E_{\text{missing}}$  final states. Not accounting for reconstruction efficiencies, estimated to be  $\simeq 60\%$  in four jet final states, the mass of charginos and neutralinos can be determined from the kinematic edges of the boson energy in inclusive SUSY event samples to a relative accuracy in the range 0.3% to 1.0% (0.6% - 1.0%) in absence of radiation and energy resolution effects to 0.8% to 1.7% (1.1% - 2.0%) accounting for ISR, BS and realistic energy resolution for the benchmark with particle masses in the range 600 - 900 GeV ( $> 1000 \text{ GeV}$ ), respectively, with  $2 \text{ ab}^{-1}$  of integrated luminosity at  $\sqrt{s} = 3 \text{ TeV}$ . The relative increase of the statistical uncertainty of the mass measurement is larger for the model I which has the sparticle masses far away from pair the production thresholds. However, in abso-



lute terms the larger production cross sections in this model yield better statistical accuracy in the mass determination. By adopting the criterion that the degradation to the mass measurement statistical accuracy from the parton energy resolution should not exceed that induced by ISR and BS, we derive the requirement of a relative energy resolution for jets,  $\delta E/E \leq 0.05$ . If the accelerator can operate at energies below the nominal  $\sqrt{s}$  (down to  $\sqrt{s}=1310$  GeV for model I and  $\sqrt{s}=2200$  GeV for model II) with comparable performance to collect about one third of the statistics at centre-of-mass energies close to the kinematic thresholds for sparticle pair production, the mass accuracies from these threshold scans improves by factors of 2 or more compared to those obtained from study of the kinematic edges at the maximum  $\sqrt{s}$  energy. The availability of polarised beam in the scan further improves these accuracies, effectively compensating for the loss of sensitivity due to the effect of ISR and beamstrahlung.

## 6 Acknowledgements

We are grateful to the colleagues who contributed to this study. In particular to Jean-Jacques Blaising, Sabine Kraml and Abdelhak Djouadi for extensive discussion and their careful reading of the text. We are also thankful to by Dieter Schlatter for valuable suggestions on this note.

## References

- [1] R.D Heuer, D. Miller, F. Richard and P.Zerwas (eds.), TESLA Technical Design Report, Part III, March 2001.
- [2] H. Stoeck *et al.* [The ILD Concept Group], The International Large Detector - Letter of Intent, March 2009.
- [3] H. Aihara *et al.* [SiD Collaboration], SiD Letter of Intent, SLAC-R-944 (2009).
- [4] Y. Li and A. Nomerotski, arXiv:1007.0698 [physics.ins-det].
- [5] G. A. Blair, A. Freitas, H. U. Martyn, G. Polesello, W. Porod and P. M. Zerwas, Acta Phys. Polon. B **36** (2005) 3445 [arXiv:hep-ph/0512084].
- [6] E. A. Baltz, M. Battaglia, M. E. Peskin and T. Wizansky, Phys. Rev. D **74** (2006) 103521 [arXiv:hep-ph/0602187].
- [7] S. Martin, private communication.
- [8] M. Battaglia, A. De Roeck, J. R. Ellis, F. Gianotti, K. A. Olive and L. Pape, Eur. Phys. J. C **33** (2004) 273 [arXiv:hep-ph/0306219].
- [9] J. R. Ellis, T. Falk, G. Ganis, K. A. Olive and M. Srednicki, Phys. Lett. B **510** (2001) 236 [arXiv:hep-ph/0102098].
- [10] A. Djouadi, J. L. Kneur and G. Moulataka, Comput. Phys. Commun. **176** (2007) 426 [arXiv:hep-ph/0211331].

- [11] M. Muhlleitner, A. Djouadi and Y. Mambrini, *Comput. Phys. Commun.* **168** (2005) 46 [arXiv:hep-ph/0311167].
- [12] G. Belanger, F. Boudjema, A. Pukhov and A. Semenov, *Comput. Phys. Commun.* **176** (2007) 367 [arXiv:hep-ph/0607059].
- [13] D. Larson *et al.*, arXiv:1001.4635 [astro-ph.CO].
- [14] T. Sjostrand, S. Mrenna and P. Z. Skands, *JHEP* **0605** (2006) 026 [arXiv:hep-ph/0603175].
- [15] F. E. Paige, S. D. Protopopescu, H. Baer and X. Tata, arXiv:hep-ph/0312045.
- [16] S. Katsanevas, P. Morawitz, *Comput. Phys. Commun.* **112** (1998) 227-269. [hep-ph/9711417].
- [17] P. Mora de Freitas, in *Proc. of the Int. Conf. on Linear Colliders (LCWS 04)*, Ed. de l'Ecole Polytechnique, Paris, 2004, vol. I, 437.
- [18] F. Gaede, *Nucl. Instrum. Meth. A* **559** (2006) 177.
- [19] A. Sailer and A. Munnich, CERN-LCD-Note-2011-002.
- [20] J. L. Feng and D. E. Finnell, *Phys. Rev. D* **49** (1994) 2369 [arXiv:hep-ph/9310211].
- [21] H. U. Martyn and G. A. Blair, arXiv:hep-ph/9910416.
- [22] F. James and M. Roos, *Comput. Phys. Commun.* **10** (1975) 343.
- [23] H. Braun *et al.* [CLIC Study Team], CLIC-NOTE-764 (2008).
- [24] M. Skrzypek and S. Jadach, *Z. Phys. C* **49** (1991) 577.
- [25] E. Boos *et al.* [CompHEP Collaboration], *Nucl. Instr. and Meth. A* **534** (2004), 250.
- [26] M. Battaglia, and J.J. Blaising, CERN-LCD-Note-2010-005, arXiv:1006.2547 [hep-ph]
- [27] M. Battaglia, E. Boos and W. Yao, eConf C010630 (2001) E3016 and arXiv:hep-ph/0111276.
- [28] S. Catani, Y. L. Dokshitzer, M. Olsson, G. Turnock and B. R. Webber, *Phys. Lett. B* **269** (1991) 432.
- [29] M. A. Thomson, *Nucl. Instrum. Meth. A* **611** (2009) 25 [arXiv:0907.3577 [physics.ins-det]].
- [30] G. A. Blair, eConf C010630 (2001) E3019.